

In situ mitigation strategies for field emission-induced cavity faults using low-level radiofrequency system*

Feng Qiu (<https://orcid.org/0000-0002-4277-2485>),^{1,2,†} Yuan He (<https://orcid.org/0000-0003-0606-2782>),^{1,2,†}
 An-Dong Wu (<https://orcid.org/0000-0003-1582-0549>),^{1,2} Zhen-Long Zhu (<https://orcid.org/0000-0001-6093-9245>),¹
 Guo-Dong Jiang,¹ Tian-Cai Jiang (<https://orcid.org/0000-0003-4218-5835>),¹ Zheng
 Gao,¹ Qi Chen (<https://orcid.org/0000-0001-7457-9666>),¹ Zong-Heng Xue,¹
 Jin-Ying Ma (<https://orcid.org/0000-0001-6366-9041>),¹ Cheng-Ye Xu (<https://orcid.org/0000-0002-3305-2988>),¹
 Zi-Qin Yang,^{1,2} and Gui-Rong Huang (<https://orcid.org/0000-0002-4815-2607>)^{1,2}

¹*Institute of Modern Physics, Chinese Academy of Sciences, Lanzhou 730000, China*

²*School of Nuclear Science and Technology, University of Chinese Academy of Sciences, Beijing 100049, China*

In the Chinese ADS front-end demo superconducting radiofrequency linac (CAFe) at the Institute of Modern Physics, a burst-noise signal-triggered cavity fault frequently appears during beam commissioning. These events are characterized by a rapid burst noise in the cavity pick-up, which may lead to an unexpected low-level radiofrequency (LLRF) response that eventually causes a cavity fault. To eliminate the undesirable reaction of the LLRF control loop, we propose a method that uses a burst-noise detection and processing algorithm integrated into the LLRF feedback controller. This algorithm can prevent undesired regulations in LLRF systems. Data analysis revealed that some burst-noise events did not exhibit measurable energy loss. In contrast, the other events were accompanied by a rapid loss of cavity stored energy and exhibited similarities to the “E-quench” phenomena reported in other laboratories. A particle-in-cell simulation indicated that the suspected E-quench phenomenon may be related to a plasma formation process inside the cavity. Fortunately, the LLRF algorithm is robust to the two different types of burst-noise events and can significantly mitigate the corresponding cavity faults in CAFe beam commissioning.

Keywords: Field emission, Flashover, E-quench, Superconducting, LLRF, CAFe, Plasma formation

I. INTRODUCTION

At the Institute of Modern Physics (IMP), a proton facility called the Chinese accelerator-driven system front-end demo superconducting radiofrequency (SRF) linac (CAFe) was built to demonstrate the possibility of a 10-mA high-power continuous-wave (CW) proton beam for the future China Initiative Accelerator-Driven System (CiADS) project [1–4]. CAFe is a 162.5-MHz SRF machine operated in the CW mode. As shown in Fig. 1, it consists of an ion source, a low-energy beam transport line (LEBT), a normal conducting (NC) radiofrequency quadrupole accelerator (RFQ), a medium-energy beam transport line (MEBT), a superconducting (SC) half-wave resonator (HWR) accelerator, a high-energy beam transport line (HEBT), and a beam dump [1]. A total of 23 SC HWR cavities, with different optimizing β (v/c) values of 0.1 and 0.15 (HWR010 and HWR015), were assembled in four cryomodules (CM₁ to CM₄). The 18 HWR010 cavities, which are denoted as CM_{M-N} (where M and N represent the number of cryomodules and the order of the cavity in each cryomodule, respectively), were installed in three identical cryomodules. Five HWR015 cavities (CM₄₋₁ to CM₄₋₅) were installed in cryomodule CM₄ [3].

Table 1 presents the main RF parameters of the six cavities in cryomodule CM3.

Availability and reliability are issues of concern for SRF-based applications, such as light-source linacs, to satisfy user expectations. For CiADS (and CAFe), reliability and availability studies are crucial. According to the operational expertise of SRF accelerator facilities worldwide, RF and cavity faults account for the majority of beam trips. Typical fault mechanisms include microphonics, transient beam loading, thermal quenching, helium fluctuations, and cavity defects associated with field emission (FE) [3, 5–11]. In particular, one type of cavity fault event, which is characterized by rapid (e.g., $\leq 7 \mu\text{s}$) and large burst noise appearing in the cavity pick-up, is one of the dominant trips at CAFe.

A burst-noise signal appeared in the pick-up probe for the four SRF cavities (CM₃₋₁, CM₃₋₃, CM₃₋₅, and CM₃₋₆) (see Fig. 1), when the same cryomodule was used. Previous studies indicated that the burst noise at CAFe involves FE-initiated discharge on the RF ceramic window surface [12, 13]. In Ref. [12], these events were attributed to an electron trapping and energy localization process in insulating materials and recognized as “flashover” events. Suspicious burst-noise signals are common and may appear in many facilities. For example, the Shanghai Synchrotron Radiation Facility (SSRF) reported a cavity fault caused by another type of burst noise (known as “arc” in SSRF) [14]. This phenomenon was interpreted as a multipacting arc in the region of the waveguide coupler. Additionally, Diamond Light Source reported burst noise (known as “cavity probe blips” in Diamond) in the cavity pick-up of two SRF cavities [15, 16]. This phenomenon was attributed to the electronic behavior of the cavity probes in Diamond. Although the formation

* This work was supported by the Strategic Priority Research Program of the Chinese Academy of Sciences (No. XDB34010000), Large Research Infrastructures China initiative Accelerator Driven System (2017-000052-75-01-000590), National Natural Science Foundation of China (No.12175283), and Studies of intelligent LLRF control algorithms for SC RF cavities (No. E129851YR0).

† Corresponding author, qiufeng@impcas.ac.cn

TABLE 1. Radiofrequency (RF) parameters of SC cavities in CM₃ for 8-mA CW beam operation.

Cavity	CM ₃₋₁	CM ₃₋₂	CM ₃₋₃	CM ₃₋₄	CM ₃₋₅	CM ₃₋₆
Cavity loaded Q (Q_L)	4.9×10^5	3.2×10^5	4.6×10^5	4.7×10^5	4.2×10^5	9.0×10^5
Cavity half-bandwidth ($f_{0.5}$) [Hz]	166	256	176	173	193	90
Cavity peak gradient (E_{peak}) [MV/m]	26	28	26	28	23	23
Transit time factor (TTF)	0.76	0.75	0.74	0.72	0.71	0.70
Synchronous phase (ϕ_s) [deg]	-34	-20	-20	-20	-20	-40
Normalized shunt impedance (r/Q) [Ω]				225		
V_c/E_{peak} [m]				0.038		
$E_{\text{peak}}/E_{\text{acc}}$				5.71		
$B_{\text{peak}}/E_{\text{acc}}$ [mT/(MV/m)]				12.52		
Maximum available power of RF source [kW]				20		
Power required for 8 mA beam operation [kW]	5.5	7.5	5.9	6.4	5.0	3.7

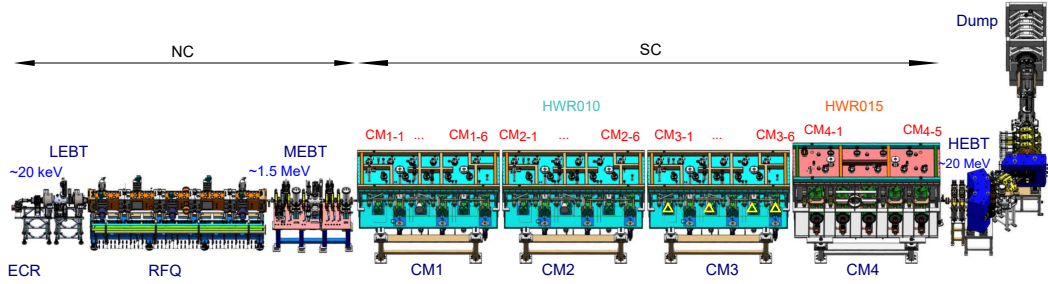


Fig. 1. (Color online) Layout of the CAFE facility. The NC and SC sections are marked in the figure. Two types of HWR superconducting cavities (HWR010 and HWR015) are mounted in four cryomodules (CM1 to CM4). The cavities CM₃₋₁, CM₃₋₃, CM₃₋₅, and CM₃₋₆ are marked by yellow triangles.

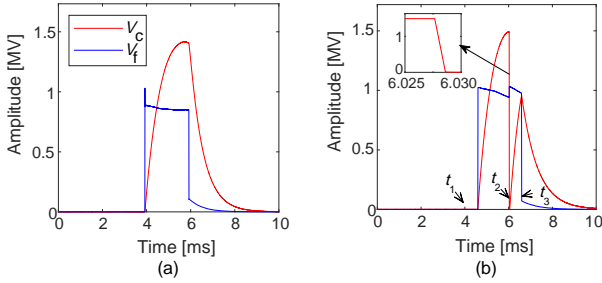


Fig. 2. (Color online) Waveforms of the RF pulse under RF conditioning in the cases (a) without E-quench and (b) with E-quench.

mechanisms for these burst noises may differ, one aspect is common: rapid and large changes in the cavity pick-up. The burst-noise signal can confuse the low-level radiofrequency (LLRF) control system, leading to undesired reactions that eventually trip the cavity.

The SSRF decreased the operation gradient to mitigate this type of cavity fault; however, this was at the expense of the accelerator's capability [14]. In CAFE, we added a cap to cover the pick-up coupler in 2019, and the burst-noise events were mitigated by 2020 [12, 13]. However, in the 2021 beam commissioning, many burst-noise events appeared in the cavity pick-up after the cavities were operated with a higher gradient. In Diamond, a 50-kHz filter was added to the LLRF control loops to suppress the burst noise (probe blips). Mean-

while, the loop gain during the period of the burst noise decreased. The risk of a trip is reduced during these activities. However, a lower gain indicates a lower ramp rate for the driver's power [15]. We propose an LLRF algorithm to address burst-noise-induced RF trips. No additional low-pass filters are required in our design; hence, the gain margin is not impacted. In addition, loop gain adjustment is not needed; therefore, the loop performance is not affected. We demonstrated the algorithm in CAFE RF and beam commissioning, and the burst-noise events did not trip the cavity, owing to the proposed LLRF algorithm.

By further inspecting the data with burst-noise events, we were surprised to see that some events did not have measurable changes in the actual cavity voltage (V_c), but other events were accompanied by a sudden (7 μ s) drop of V_c . The cavity stored energy W can be calculated as follows [17]:

$$W = \frac{V_c^2}{\omega_0(r/Q)}, \quad (1)$$

where ω_0 and r/Q represent the cavity resonant frequency and the normalized shunt impedance, respectively. Because ω_0 and r/Q are approximately invariant at the μ s scale, the V_c drop corresponds to an energy loss. Events without energy loss are consistent with the flashover phenomena described in Ref. [12]. However, other events with energy loss are unexplained. Similar phenomena with complete rapid energy loss, which are referred to as E-quench, have been reported

in many facilities, such as KEK [18], JLAB [19], and DESY [9]. In CAFE, we also observed suspected E-quench phenomena during pulsed RF conditioning on CM₃₋₅ [3]. In Fig. 2, RF pulses with and without the suspected E-quench phenomena are presented. The stored cavity energy was completely lost in 1 μ s [see Fig. 2(b)]: In this study, we suspect that a burst-noise event with partial energy loss is a type of mini-E-quench. Fortunately, the proposed LLRF algorithm is robust to the two different burst-noise events.

II. LLRF AND ALGORITHM

Figure 3 presents the waveform of the burst noise in CAFE. Two typical burst-noise patterns were observed. Although the duration and shape differed, these burst-noise signals were large enough to confuse the LLRF system and lead to an undesired proportional–integral (PI) FB loop reaction. Details regarding the field-programmable gate array (FPGA)-based LLRF system can be found in [5, 20]. A burst-noise detection and processing module was built into the LLRF control loops, as shown in Fig. 4. This module aimed to remove the cavity faults induced by burst noise, which is discussed in detail in this section. An embedded Linux system was installed on an ARM chip integrated into the FPGA. The Experimental Physics and Industrial Control System (EPICS) was installed on the Linux system to achieve data acquisition.

Initially, we followed the activities of Diamond and considered applying a digital low-pass filter to suppress burst noise. Two additional low-pass filters $H_{\text{fil}}(s) = \alpha^2 / (s + \alpha)^2$ were introduced in the LLRF control loops (after the CORDIC module in Fig. 4). The parameter α was used to regulate the filter bandwidth. The simulation results are presented in Fig. 5. As shown, the filters improved the signal quality—particularly for the amplitude loop. The amplitude fluctuation was reduced to $\pm 5\%$ in the presence of the filter with a 20-kHz 3-dB bandwidth. However, the phase fluctuation remained larger than 40° under the same conditions. This indicated that the phase may be flipped by 180° even with a low FB gain of 5. Therefore, the risk of an RF trip on the reflected power remains.

In addition, we investigated the impact of the filter on the gain margin by checking the open-loop Bode plots. In CAFE, the cavity half-bandwidth ($f_{0.5}$) is far smaller than those of the other RF components in the control loop. In our case, the cavity itself contributes only to the dominant poles. Furthermore, we assume that there is no coupling between the control objects [i.e., the cavity detuning (Δf) is well compensated, and the loop phase is well calibrated]. Under these assumptions, the open-loop transfer function of the LLRF system without a filter (H_1) and with a filter (H_2) can be simplified

as

$$\begin{cases} H_1 = \frac{2\pi f_{0.5} \cdot G_{\text{ol}} \cdot e^{-T_d s}}{s + 2\pi f_{0.5}}, \\ H_{\text{fil}} = \frac{\alpha^2}{(s + \alpha)^2}, \\ H_2 = H_1 \cdot H_{\text{fil}} \end{cases} \quad (2)$$

The open-loop Bode plots in Fig. 5(b) indicate that the filter significantly reduced the PM in FB control with a lower bandwidth.

TABLE 2. Control parameters for the simulation in Fig. 5(b).

Item	Value
Loop gain, G_{ol}	50
Loop delay, T_d (μ s)	1.5
Cavity half-bandwidth, $f_{0.5}$ (Hz)	176

The simulation study indicated that the low-pass filter can attenuate noise but creates new problems. In this section, we propose a “burst-noise detection and processing” algorithm. Because the burst-noise signal is typically characterized by large and rapid changes in the cavity pick-up signal, it can be detected by applying a simple digital differentiator in the LLRF loop, as shown in Fig. 6(a). The differentiator is used to compute the difference between successive pick-up signal samples. If the absolute value of the difference signal exceeds a predefined threshold, a burst-noise trigger signal (T1) is activated and maintained for a time interval ΔT . In our case, the time period ΔT is typically set as 15 μ s, which is longer than the duration of burst noise (which is generally 10 μ s). Determination of the threshold value is another critical issue. This value cannot be too small; otherwise, accidental random analog-to-digital converter (ADC) noise can be falsely identified as burst noise. Conversely, if the value is too large, the LLRF system has already responded unexpectedly. In CAFE, the threshold is selected to be approximately 10 times the typical ADC noise amplitude.

A large error signal was sent to the PI FB controller when burst-noise events occurred, leading to an unexpected loop response and eventually causing a cavity fault. A burst-noise processing model is integrated into the PI controller to avoid system collapse. As shown in Fig. 6(b), the trigger “T1” first turns switch “ S_1 ” to the upper position to prevent the arrival of the large errors arising from the burst-noise events. In this case, the input of the PI controller is connected to a zero register. This activity can prevent unwanted data accumulation of the accumulator “ACC” in the I controller. However, part of the error signal can enter the PI controller before the trigger is emitted (see Fig. 7). To solve this problem, another switch, i.e., “ S_2 ,” is temporally switched to a latch (upper position) until the trigger “T1” returns to 0 state. The latch circuit always retains the data from the PI output data of 0.8 μ s prior to the rising edge of the burst-noise trigger. Meanwhile, the value in the accumulator “ACC” is replaced by the data in the



chinaXiv:202306.00124v1



chinaXiv:202306.00124v1

chinaXiv:202306.00124v1

chinaXiv:202306.00124v1

chinaXiv:202306.00124v1

chinaXiv:202306.00124v1

chinaXiv:202306.00124v1

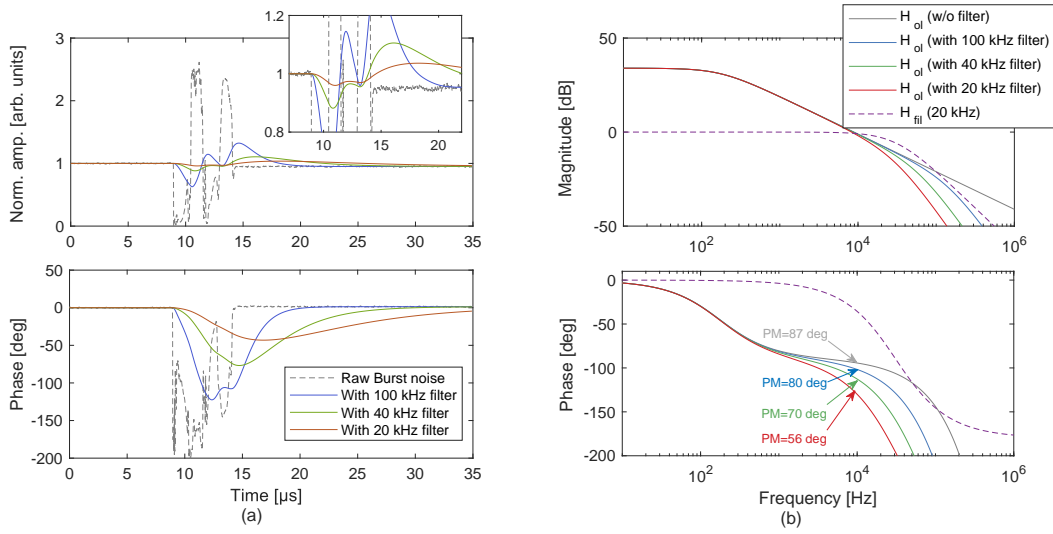


Fig. 5. (Color online) (a) Comparison of the raw and filtered burst-noise signals. The filters used were 2nd-order infinite impulse response filters with the same form H_{fil} but different 3-dB bandwidths. The burst-noise-induced amplitude fluctuation was reduced to $\pm 5\%$ in the presence of the 20-kHz filter. However, the phase fluctuation remained larger than 40° . (b) Comparison of the open-loop Bode diagrams for the cases without filters and with filters of different 3-dB bandwidths. For clarity, the frequency response of the 20-kHz 2nd-order filter is shown as well. The filters significantly affected the system phase-margin (PM) values, which are marked in the phase diagram.

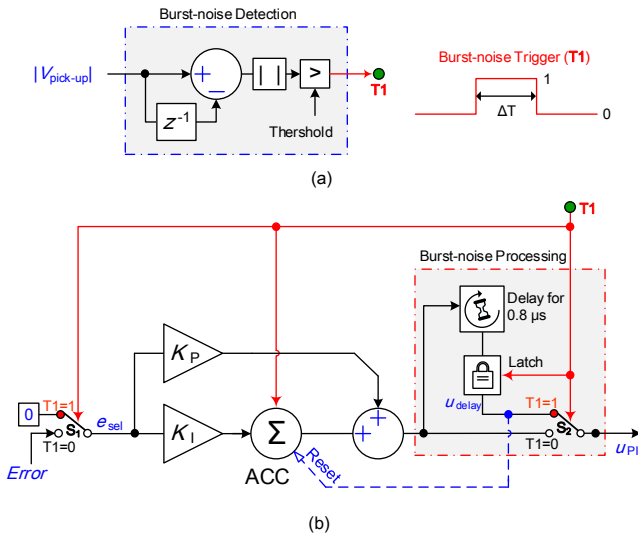


Fig. 6. (a) Schematic of the burst-noise detection algorithm. (b) Schematic of the burst noise processing algorithm.

nal with and without the proposed algorithm, and Fig. 8(b) shows the corresponding PI outputs. First, we fed the system without an algorithm. The burst noise led to undesired PI regulation and eventually tripped the cavity (indicated by black). Next, we activated the algorithm and evaluated its performance. When burst noise was detected, the PI regulation was immediately suspended for $15 \mu\text{s}$ (indicated by red). The overall response process was consistent with the schematic presented in Fig. 7.

Additionally, we validated the proposed algorithm in the presence of a beam. We activated the algorithm and operated

CAFe with an 8-mA CW beam continuously for 108 h. The RF parameters are presented in Table 1. The gradients of cavities CM_{3-1} , CM_{3-3} , CM_{3-5} , and CM_{3-6} were limited by frequent burst-noise interference. Furthermore, the gradient of cavity CM_{3-5} was limited by the E-quench at approximately 25 MV/m, although the reason remains unclear. The gradient of cavity CM_{3-6} was limited by thermal breakdown at approximately 27 MV/m. During the beam commissioning, we reduced the peak cavity gradients of these two cavities to 23 MV/m to achieve safe beam operation. The loop gains of the LLRF system were set between 30 and 60 (depending on the cavity half-bandwidth) to ensure a gain margin of $> 20 \text{ dB}$ and a closed-loop bandwidth of approximately 10 kHz. RF faults were not observed after the implementation of the proposed algorithm. Figure 9 presents the RF stability, the beam current signal, and the corresponding burst-noise trigger signal for cavity CM_{3-1} over 24 h.

As discussed in Sect. IV, certain burst-noise events (i.e., mini-E-quench events) take cavity stored energy and lead to field drops. In practice, to ensure uninterrupted 8-mA beam operation, we set a relatively loose threshold for the maximum tolerable burst noise-induced RF fluctuation ($20 \mu\text{s}$ after the burst noise passes away). The threshold is 2.5 MV/m for the field amplitude and 2.5° for the phase. If the burst noise-induced amplitude and phase changes are below the threshold, the LLRF interlock is not sent out, and the beam is operated without suspension. Because the RF source rapidly compensates for the field drop with a typical timescale of $200 \mu\text{s}$, the beam loss caused by these types of burst-noise events is acceptable. Fortunately, the cryogenic load challenge was absent in the field drop process of CAFe. A rapid change in the cavity field leads to an increase in Lorentz force detuning, which affects the cavity phase [21]. This phenomenon was

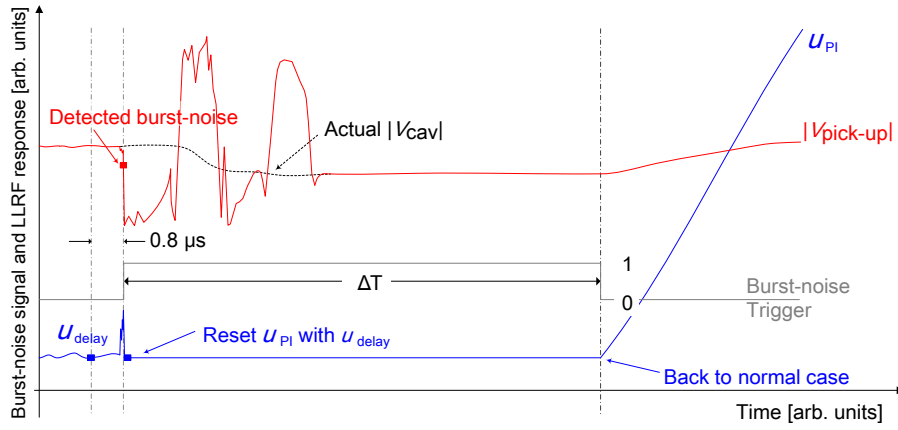


Fig. 7. (Color online) Principle of the burst-noise detection and processing algorithm. When the LLRF system detects the burst-noise events (indicated by the red square), a burst-noise trigger is immediately emitted and is held for a time interval of ΔT . The PI output of u_{PI} is overwritten by u_{delay} (the blue square on the left side), which retains the data from u_{PI} $0.8 \mu s$ prior to the rising edge of the burst-noise trigger.

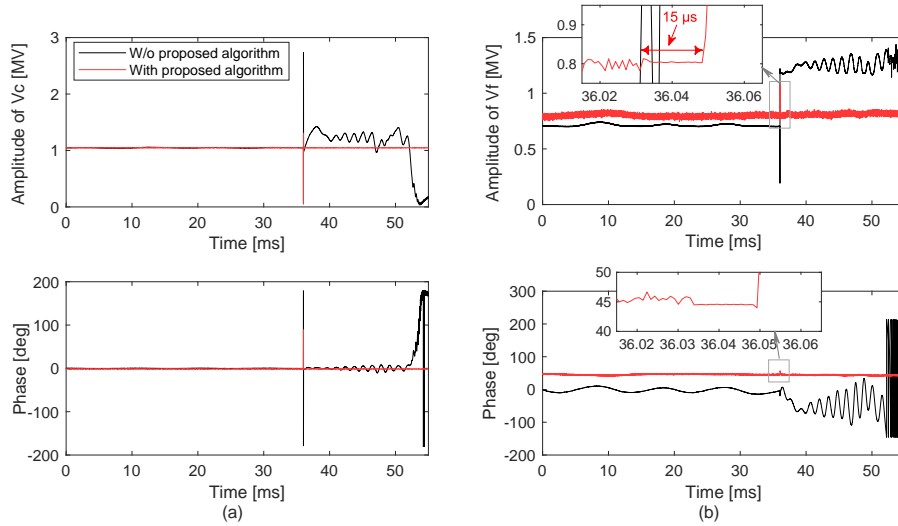


Fig. 8. (Color online) Performance of the proposed burst-noise detection and processing algorithm. (a) Amplitude and phase of the cavity pick-up signal in the cases with (red) and without (black) the proposed algorithm. (b) Amplitude and phase of the LLRF output in the cases with (red) and without (blue) the proposed algorithm.

observed at CM_{3-3} and CM_{3-6} . Nevertheless, availabilities of 94% for the CW beam and 98% for the SRF cavity were achieved in CAFe beam commissioning. As indicated by its success in CAFe, this algorithm can be extended to other CW accelerators that suffer from burst-noise perturbation.

Figure 10 shows the overall number of burst-noise triggers over 108 h. It was found that cavities CM_{3-1} and CM_{3-5} frequently triggered burst noise. However, LLRF interlock signals were rare. This indicated that most of the amplitude and phase fluctuations caused by the burst-noise events were below the given threshold, which is clarified in Fig. 14 and Sect. V. To investigate the relationship between the occurrence rate of burst-noise events and the cavity gradient, we temporarily increased the cavity gradient by several millivolts per meter and examined the increment in burst-noise

events. The results are shown in Fig. 10. The occurrence rate of events increased with the cavity gradient. This result motivated us to correlate the initial mechanism of burst-noise events with the FE.

IV. DISCUSSION

Through the proposed LLRF algorithm, the cavity faults induced by the two different types of burst noise were eliminated. Thus, it is possible to further analyze the fault data and investigate the possible intrinsic physical mechanisms. Although the cavity pick-up may be polluted by burst noise and cannot reflect the actual cavity field, it is possible to reconstruct the actual V_c with other clean signals. For example,

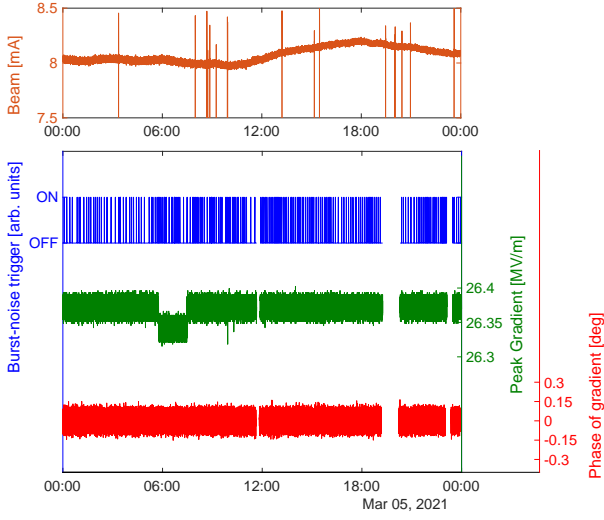


Fig. 9. (Color online) Long-term operation of cavity CM_{3-1} during the beam commissioning. The blue spike signals indicate the burst-noise events (ON: burst-noise signal appears). The missing samples in the signal are mainly caused by LLRF data communication failure. According to the recorded data of the cavity field, the cavity faults are effectively removed. Spikes are observed in the beam current signal (upper plot), but they are not correlated with the burst-noise events.

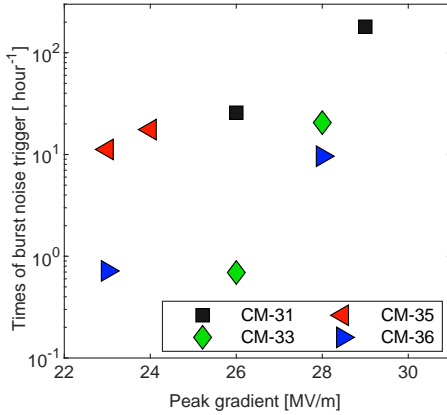


Fig. 10. (Color online) Occurrence rate of the burst-noise events in four of the SC cavities at CAFE.

according to Refs. [20, 22–24],

$$V_c = V_f + V_r \quad (3)$$

Here, the actual V_f and V_r can be calibrated from the measured cavity forward and reflected signals (V_f^* and V_r^*) as follows:

$$V_c = XV_f^* + YV_r^* \quad (4)$$

According to the algorithm described in Refs. [20, 23], the two complex constants X and Y can be calibrated using the waveform data from the pulsed mode. Figure 11 presents a

comparison of the measured V_c and reconstructed V_c values, and the results indicate good consistency. The actual cavity gradient can be calibrated using the known X and Y . Figure 12 shows a comparison of the calibrated V_c and measured V_c values for the two types of burst-noise events. The cavity gradient remains stable in Fig. 12(a) but significantly decreases in Fig. 12(b).

The energy loss shown in Fig. 12(b) is gradually compensated for by LLRF FB. The cavity Q_L and cavity detuning ($\Delta\omega$) can be estimated in this power filling process using the formula

$$\begin{cases} \omega_{0.5} = \frac{\frac{d|V_c|}{dt}}{2|V_f|\cos(\theta - \phi) - |V_c|}, & Q_L = \frac{\omega_{RF}}{2\omega_{0.5}} \\ \Delta\omega = \frac{d\phi}{dt} - \frac{\omega_{0.5}(|2V_f|\sin(\theta - \phi))}{|V_c|}, \end{cases} \quad (5)$$

where θ and ϕ represent the phases V_c and V_f , respectively. The parameters ω_{RF} and $\omega_{0.5}$ represent the RF frequency and cavity half-bandwidth, respectively. Figure 13(a) shows the calibrated Q_L obtained using the waveform data from Fig. 12(b). The Q_L of approximately 9×10^5 in Fig. 13(a) is consistent with the Q_L measured from the field decay curve when the RF was turned off. Because the cavity gradient changes rapidly, Lorentz force detuning may appear after the event, as shown in Fig. 13(b). The detuning frequency was approximately 200 Hz, which was consistent with that of the cavity mechanical modes. This finding confirms that the actual energy was partially lost in the event presented in Fig. 12(b).

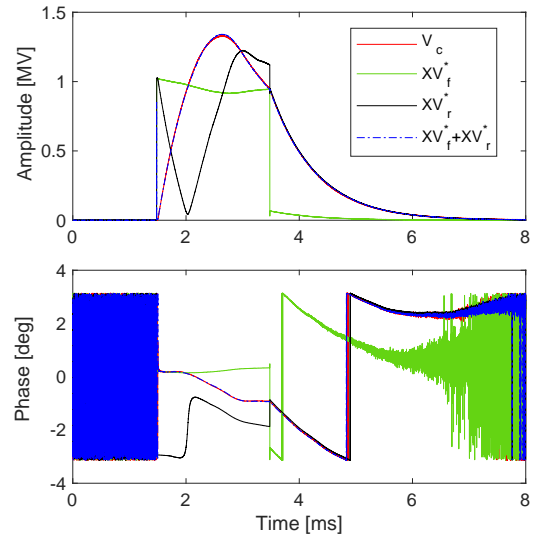


Fig. 11. (Color online) Comparison of measured V_c and calibrated V_c values obtained using V_f^* and V_r^* for cavity CM_{3-5} .

Further data analysis indicated that all the cases shown in Fig. 3(a) exhibited no gradient drop, but all the cases in Fig. 3(b) involved the gradient drop. As reported in Ref. [12], the events shown in Fig. 3(a) are flashover phenomena that involve discharge on the surface of the RF ceramic window of

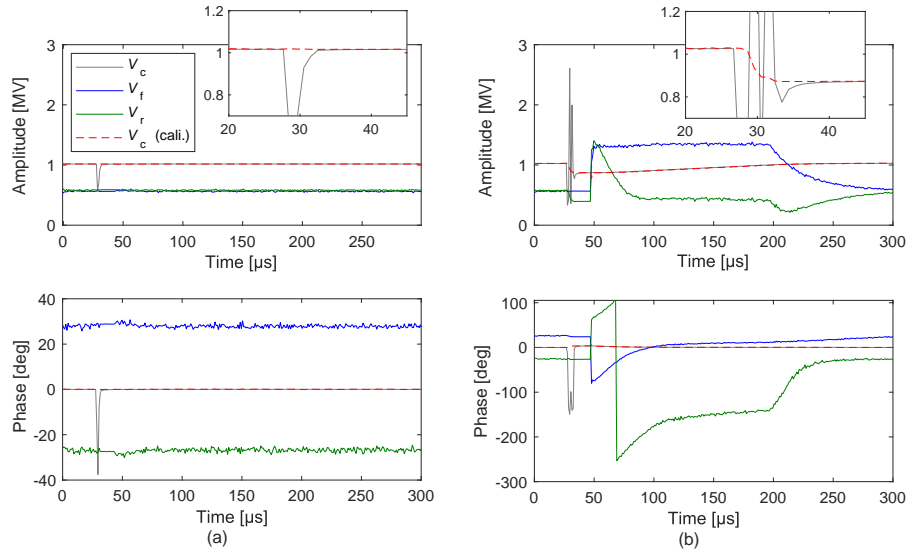


Fig. 12. (Color online) Separation of actual V_c from the cavity pick-up merged with the burst-noise signal in the case with the proposed algorithm under FB control.

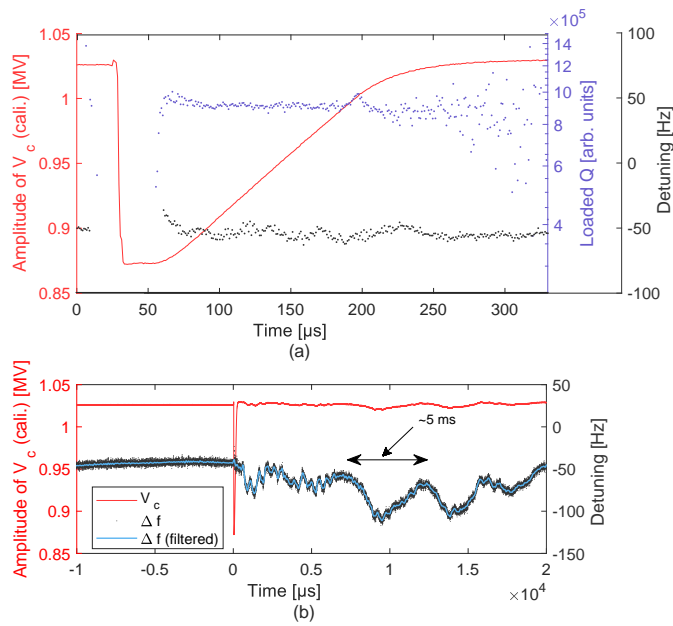


Fig. 13. (Color online) (a) Calibration of the cavity loaded Q (Q_L) using the waveform data from the energy filling time. The calibrated Q_L was approximately 9×10^5 , which is consistent with the Q_L extracted from the field decay curve. (b) Cavity detuning (caused by rapidly changing cavity gradient) before and after the mini-E-quench event. The ~ 200 -Hz fluctuation is consistent with one of the cavity mechanical modes.

the pick-up coupler. Because the pick-up coupler is located in an area with a low energy density, this discharge in the RF window does not consume the cavity energy. The interpretation in Ref. [12] is consistent with the event characteristics shown in Fig. 3(a). For the events in Fig. 3(b), we considered the possibility of attrition of the phenomena to the discharge

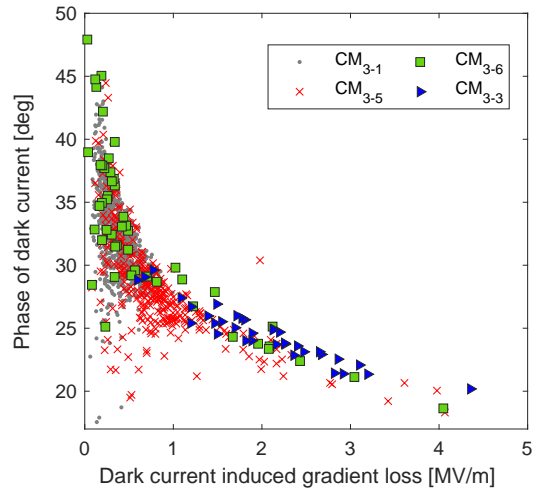


Fig. 14. (Color online) Phase of the dark current as a function of the dark current-induced field loss. The plots for the four cavities in which the mini-E-quench events appeared obey similar rules.

TABLE 3. Characteristics of E-quench, mini-E-quench, and flashover.

Item	E_{peak} range (MV/m)	Gradient loss	Burst-noise duration (μm)
Flashover	15 \sim 20	Negligible	~ 4
Mini-E-quench	20 \sim 25	2% \sim 20%	~ 7
E-quench	>30	100%	~ 1

behavior inside the cavity. Similar phenomena with a sudden and complete loss of the cavity stored energy have been recorded in many facilities, such as KEK, JLAB, DESY, and CAFE. JLAB called this phenomenon “E-quench” and inter-

preted it as the effect of releasing a large number of electrons inside the cavity, which absorb the cavity energy. The events with partial cavity energy loss exhibited similar behavior to the E-quench phenomena. Owing to the lack of sufficient direct evidence, we hypothesize that the phenomena in Fig. 3(b) indicate the electron emission behavior inside the cavity. In this paper, we categorize burst-noise events with partial energy loss as “mini-E-quench”. According to our experience with CAFe, we summarize the characteristics of flashover, mini-E-quench, and E-quench in Table 3.

The abnormal electrons emitted inside the RF cavity are typically referred to as dark current. The dark-current-induced RF transient shown in Fig. 12(b) can be interpreted as a type of beam loading. It is possible to extract beam information (i.e., beam current and beam phase) from the beam-induced RF transient (see Appendix A) [23, 25–27]. Figure 14 shows a comparison of the phases of the dark current as a function of gradient loss in the four cavities with burst-noise events. Interestingly, the plots of all events indicate similar distribution patterns that appear to be independent of the cavity. The reason for this phenomenon remains unclear. Because the mini-E-quench events never appeared in cavities CM₃₋₂ and CM₃₋₄ or in the cavities mounted in other cryomodules (except for CM₃), it is not presumed that a dark current on a cavity upstream was transmitted to the cavities downstream. Further analysis of the dark current-induced transient suggested that the dark current probably had a two-peak shape (a large peak followed by a smaller peak). A detailed analysis is presented in Appendix A.

To further investigate the possible source of the dark current, a particle-in-cell (PIC) simulation was performed in the HWR010 cavity using CST Particle Studio. The simulation results indicated that the mini-E-quench phenomenon was mostly linked to plasma-formation events inside the cavity (see Appendix B).

V. OUTLOOK

Another possible solution to the burst-noise issue is to replace the polluted cavity pick-up signal with the calibrated V_c signal (i.e., $V_c = XV_f^* + YV_r^*$) in the FPGA. As shown in Fig. 12, burst noise did not appear in the calibrated signal. Therefore, the burst-noise processing algorithm in Fig. 6 is generally not required. Another advantage of this method is that we can directly identify suspected mini-E quench events by appropriately modifying the burst-noise detection algorithm. The calibration factors X and Y may be affected by other quantities, such as the cavity forward power or temperature drift, but this is beyond the scope of the present study.

The hypothesis regarding mini-E-quench and flashover presented in Sect. IV lacks direct evidence. Therefore, a fast radiation detector is necessary. Several activities can be performed in future studies to confirm our hypotheses. One possible solution is to replace the current pick-up coupler with a magnetic coupling pick-up coil in a high-magnetic field area that is far from the high-electric field area. The electron and ion bombardment rates in the pick-up coupler may be signif-

icantly reduced, and the burst-noise issue may be mitigated.

VI. CONCLUSION

In CAFe, two different types of burst-noise signals confuse the LLRF system, leading to an undesired reactions and eventually causing cavity fault. We developed a burst-noise detection and processing algorithm and integrated it into the LLRF control loop to avoid undesired LLRF FB regulation. Data analysis indicated that one type of burst-noise event is associated with significant gradient loss, whereas the other type is without gradient loss. We categorized the burst-noise events as flashover (without energy loss) and mini-E-quench (with partial energy loss) accordingly. The proposed algorithm eliminated cavity faults caused by both types of burst noise in CAFe beam commissioning. Further analysis indicated that the gradient loss in the mini-E-quench event and the corresponding dark-current phase obeyed the specified distribution rules. The reasons for this phenomenon remain unclear. A PIC simulation suggested that the mini-E-quench is probably linked to a plasma-formation event.

VII. ACKNOWLEDGMENTS

We thank all the members of the CAFe commissioning team for providing stable beam operation. We also thank all the operation staff members for their cooperation and help during the machine study.

VIII. AUTHOR CONTRIBUTIONS

All authors contributed to the study conception and design. Material preparation, data collection and analysis were performed by Feng Qiu, Yuan He and An-Dong Wu. The first draft of the manuscript was written by Feng Qiu and all authors commented on previous versions of the manuscript. All authors read and approved the final manuscript.

IX. APPENDIX

A. Appendix A: Approach for characterizing dark current

We can obtain the beam information according to the beam-induced RF transient. This principle is explained in Fig. 15. The amplitude and phase of the transient field induced by the beam are shown in Fig. 15(a). The short blue lines represent the cavity field before the beam arrival. The red line represents the beam-induced transient when the beam passes through the cavity. The short green lines depict the case where the beam ends. The cavity field is a superposition of the generator-induced field and the beam-induced field within this moment. Accordingly, the beam transient vector was geometrically added to the cavity field in Cartesian coordinates. The beam phase (ϕ_b) can be obtained by

computing the angle between V_c (the moment before the arrival of the beam) and the beam transient vector, i.e., ΔV_{ind} [see Fig. 15(b)]. Additionally, the length of ΔV_{ind} is directly proportional to the beam intensity.

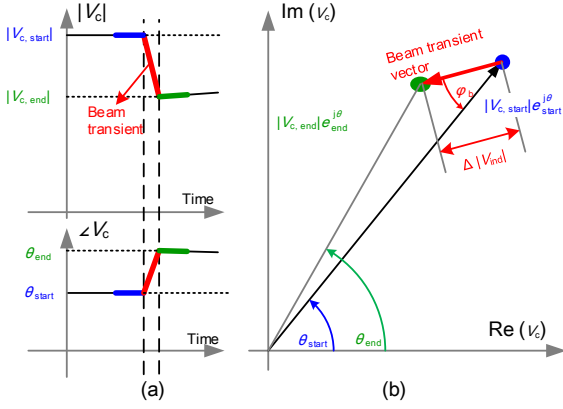


Fig. 15. (Color online) Principle for characterizing the beam phase using a beam-induced transient signal. (a) Amplitude and phase of the cavity field with the beam-induced transient. (b) Cavity voltage in Cartesian coordinates. The red arrow indicates the beam transient vector.

Figure 16(a) shows the amplitude and phase (A/P) waveform of the peak gradient on CM₃₋₃ for four different mini-E-quench events. The corresponding I/Q components in Cartesian coordinates are shown in Fig. 16(b). The phase between the dark current and the cavity field can be calibrated using the aforementioned method. ΔV_{ind} can be obtained by fitting a linear equation to the RF transient:

The dark-current profile can be roughly estimated from the dark current-induced transient using the cavity differential equation [17, 23, 28]

$$\frac{dV_c}{dt} + (\omega_{0.5} - i\Delta\omega)V_c = \omega_{0.5}(2V_f + 2V_b) \quad (6)$$

where V_f and V_b represent the forward and current-induced voltages, respectively. To increase the signal-to-noise ratio of the waveform data, we deliberately selected a mini-E-quench event that caused a gradient loss of 9 MV/m in cavity CM₃₋₃ (not shown in Fig. 14). The estimated current profiles are shown in Fig. 17. Interestingly, the dark current exhibited a two-peak shape (a larger peak followed by a smaller peak). The maximum dark current during this event was approximately 2.4 A. In this calibration, we used a transit time factor of 0.7, which is the optimized value for the HWR010 cavity. The actual peak dark current should be > 2.4 A (because the speed of the electrons changes on a large scale). The data analysis indicated that for all the events in Fig. 14, the dark currents had similar two-peak shapes with different phases and intensities.

B. Appendix B: PIC simulation

When the HWR010 cavity was operated at its fundamental mode frequency, the maximum electric field was located in the inner conductor, as shown in Fig. 18(a). Therefore, electrons were most likely emitted from the inner conductor, as shown in Fig. 18(b). The emitted electrons are then accelerated in the electric field and collide with the outer surface of the cavity. In the CST PIC solver, we selected a face emitter in the inner conductor. The field-emitted current density, i.e., j_{FE} , conforms to Fowler-Nordheim (FN) theory [29, 30] and can be expressed as

$$j_{\text{FE}} = \frac{1.54 \times 10^{-6} \times 10^{4.52\phi - 0.5} \beta_{\text{FN}}^2 E_s \cos(\omega_{\text{RF}} t)}{\phi} e^{-\frac{6.53 \times 10^9 \phi^{1.5}}{\beta_{\text{FN}} [E_s \cos(\omega_{\text{RF}} t)]^2}} \quad (7)$$

where parameter ϕ represents the work function of the material in eV (for niobium, $\phi = 4.3$ eV), E_s represents the surface electric field. The parameter β_{FN} is the enhancement factor, which describes the ratio of the local electric field to the average surface field. In the PIC simulation, we selected two enhancement factors: $\beta_{\text{FN}}=130$ and $\beta_{\text{FN}}=1000$. In Fig. 19, the dark blue curve shows the distribution of the initial field-emitted current. The red curve indicates the current at which the emitted electrons collide with the outer conductor. The RF field was also plotted, for comparison. As shown in Fig. 19, the maximum phase between the FE current and RF was approximately 12° . This is inconsistent with the results presented in Fig. 14, which indicate a dark-current phase between 15° and 50° .

Another possible source of the dark current is plasma formation. The FE current ionizes the absorbed gas, and a dense plasma sheath is formed around the emitter on a short timescale (sub-microsecond). This process is consistent with the arcing mechanism in an RF device [31]. The plasma creates an electric field on the local RF surface that can reach GV/m levels [32], making it far stronger than the RF field (e.g., $E_{\text{peak}} < 30$ MV/m in CAFe). The FE current increases exponentially with an increase in the field strength. Here, the dark current is mainly contributed by the field-emitted electrons (on the local RF surface) and ions in the dense plasma. The current density (which is limited by the space charge effects) can reach 10^{12} A/m². As shown in Fig. 14, the estimated dark current was approximately 0.1~1 A, corresponding to an emissive area of 0.1~1 μm^2 , which is consistent with Refs. [31, 33]. Many smaller droplets and debris are ejected and randomly distributed near the FE site with the explosion of the original emitters (e.g., projection and particles) on the RF surface. The smaller droplets and debris may create a new plasma cloud and trigger a secondary chain of events. The two peaks in Fig. 19 may correspond to two successive plasma-formation events. The main peak was caused by the explosion of the original emitter. In contrast, the sub-peak was probably due to the second plasma-formation event related to the smaller debris created by the explosion of the original emitters. Finally, the electrons and positive ions from two successive plasma-formation events may collided with the pick-up antenna. Consequently, the cavity pick-up signal rapidly jumped up and down. According to the foregoing analysis, we conclude that the mini-E-quench events are most

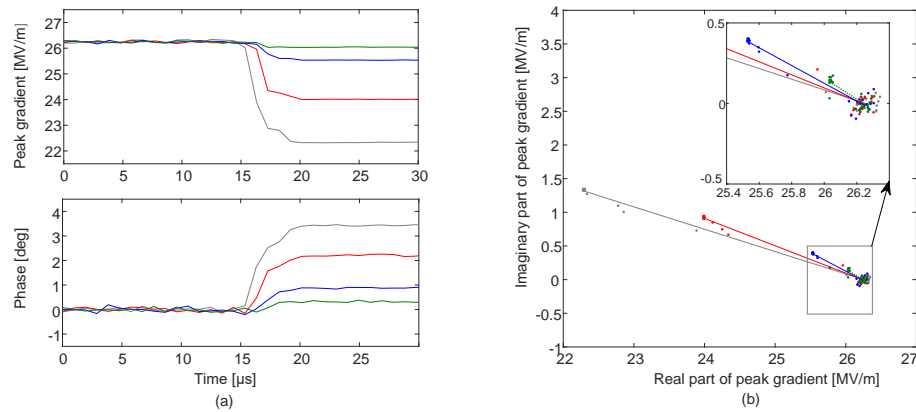


Fig. 16. (Color online) (a) Calibrated amplitude and phase waveform of the cavity field of CM_{3-3} for the four different mini-E-quench events. (b) Corresponding in-phase and quadrature (I/Q) components in Cartesian coordinates.

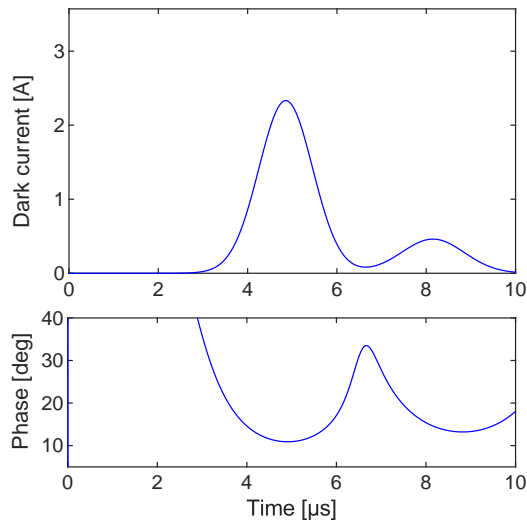


Fig. 17. Estimated dark-current profile based on the dark current-induced transient.

likely linked to the plasma-formation events inside the cavity rather than the ceramic window.

-
- [1] Z. J. Wang, Y. He, H. Jia et al., Beam commissioning for a superconducting proton linac. *Phys. Rev. Accel. Beams* **19**, 120101 (2016). DOI: <https://doi.org/10.1103/PhysRevAccelBeams.19.120101>
 - [2] S.H. Liu, Z.J. Wang, H. Jia et al., Physics design of the CIADS 25 MeV demo facility. *Nucl. Instrum. Methods Phys. Res. A* **843**, 11–17 (2017). DOI: <https://doi.org/10.1016/j.nima.2016.10.055>
 - [3] Y. He, Operation Experience at CAFE, in *oral presentation of 2021 International Conference on RF Superconductivity (SRF'21)*, virtual conference, 28 June–2 July 2021, edited by JACoW editor team (JACoW, virtual conference, 2021).
 - [4] Q. Chen, Z. Gao, Z.L. Zhu et al., Multi-frequency point supported LLRF front-end for CiADS wide-bandwidth application. *Nucl.Sci. Tech.* 31(3), 29 (2020). DOI: 10.1007/s41365-020-0733-9
 - [5] F. Qiu, S. Michizono, T. Matsumoto et al., Combined disturbance-observer-based control and iterative learning control design for pulsed superconducting radio frequency cavities. *Nucl. Sci. Tech.* **32**, 56 (2021). DOI: 10.1007/s41365-021-00894-y
 - [6] N. Walker, D. Reschke, J. Schaffran et al., *Performance analysis of the European XFEL SRF cavities from vertical test to operation in modules*, in *Proceedings of 28th International Linear Accelerator Conference (LINAC2016)*, East Lansing, MI, USA, 25–30 September, edited by JACoW editor team (JACoW, East Lansing, MI, USA, 2016), pp. 657–662.
 - [7] T. Powers and A. Solopova, *CEBAF C100 Fault classification based on time domain RF signals*, in *Proceedings of the 19th International Conference on RF Superconducting (SRF2019)*, Dresden, Germany, 30 June–5 July 2019, edited by JACoW editor team (JACoW, Dresden, Germany, 2019), pp. 763–769.
 - [8] C. Tennant, A. Carpenter, T. Powers et al., Superconducting radio-frequency cavity fault classifica-

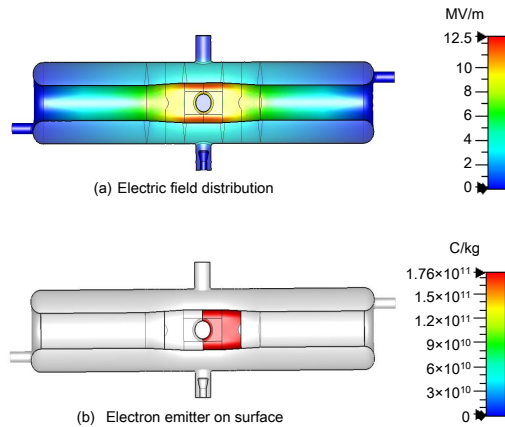


Fig. 18. (Color online) (a) Electric-field distribution in an HW010 cavity. (b) The inner conductor (indicated by the red area) is selected as the face-emitter in the CST PIC server.

tion using machine learning at Jefferson Laboratory. Phys. Rev. Accel. Beams **23**, 114601 (2020). DOI: <https://doi.org/10.1103/PhysRevAccelBeams.23.114601>

- [9] M. Omet, Exceptional events during the operation of the european XFEL, in *oral presentation of 2019 TESLA Technology Collaboration (TTC2019)*, Vancouver, Canada, 5-8 February, 2019, edited by B. Laxdal (TRIUMF, Canada, 2019). Available at <https://indico.desy.de/event/21337/timetable/?view=standard>
- [10] J. Branlard, Automation algorithms for LLRF operation, in *oral presentation of 2019 LLRF workshop*, Chicago, US, 29 September-03 October 2019 (Fermilab and Argonne National Laboratories, US, 2019).
- [11] F. Qiu, S. Michizono, T. Miura et al., Application of disturbance observer-based control in low-level radio-frequency system in a compact energy recovery linac at KEK. Phys. Rev. ST Accel. Beams **18**, 092801 (2015). DOI: <https://doi.org/10.1103/PhysRevSTAB.18.092801>
- [12] X.M. Liu, Y. He, Y. M. Li et al., Detection and suppression of the trapped-electrons-transportation-type flashover in a linear accelerator. Phys. Scr. **96**, 105301 (2021). DOI: 10.1088/1402-4896/ac0c91
- [13] X. M. Liu, Y. He, G. R. Huang et al., Flashover on RF window of HWR SRF cavity, in *Proceedings of 19th International Conference on RF Superconductivity (SRF2019)*, Dresden, Germany, 30 June-5 July 2019, edited by JACoW editor team (JACoW, Dresden, Germany, 2019), pp. 597-599.
- [14] H. T. Hou, J. F. Liu, Y. B. Zhao et al., Analysis of superconducting cavity quench events at SSRF. Chin. Phys. C **35**(2), 179 (2011). DOI: 10.1088/1674-1137/35/2/014
- [15] P. Gu, M. R. F. Jensen, M. J. Maddock et al., Reliability improvements of the Diamond superconducting cavities, in *Proceedings of 15th International Conference on RF Superconductivity (SRF2011)*, Chicago, US, 25-29 July, 2011, edited by JACoW editor team (JACoW, Chicago, USA, 2011), pp. 267-270.
- [16] P. Gu and M. Peter, RF Progress at Diamond Light Source, in *Oral presentation of 19th ESLS-RF Workshop*, Lundt, Sweden, 30 September-1 October, 2015 (MAX IV Laboratory, Lundt, Sweden, 2015). Available at <https://www.cells.es/en/media/workshops/european-synchrotron-rf-meetings/19th-esls-rf-meeting>
- [17] T. Schilcher, Vector sum control of pulsed accelerating fields in Lorentz force detuned superconducting cavities, Dissertation for the Doctoral Degree (Universitt Hamburg, Hamburg, 1998).
- [18] K. Akai, Performance of SRF systems in storage rings, in *Proceedings of the fifth Workshop on RF Superconductivity (SRF91)*, DESY, Hamburg, Germany, 19-23 August 1991, edited by D. Proch (DESY, Hamburg, Germany, 1991), pp. 126-137.
- [19] T. Powers, L. R. Doolittle, P. Kneisel et al., *Investigations of arcing phenomena in the region near CEBAF RF windows at 2 K*, in *Proceedings of the sixth Workshop on RF Superconductivity (SRF93)*, CEBAF, Newport News, Virginia, USA, 4-8 October 1993, edited by R. M. Sundelin (CEBAF, Virginia, USA 1993), pp. 1-18. Available at <https://accelconf.web.cern.ch/SRF93/papers/srf93k01.pdf>
- [20] J. Y. Ma, F. Qiu, L. B. Shi et., Precise calibration of cavity forward and reflected signals using low-level radio-frequency system. Nucl. Sci. Tech. **33**, 4 (2022). DOI: 10.1007/s41365-022-00985-4
- [21] F. Qiu, Z. L. Zhu, J. Y. Ma et al., An approach to characterize Lorentz force transfer function for superconducting cavities. Nucl. Instrum. Methods Phys. Res. A **1012**, 165633 (2021). DOI: <https://doi.org/10.1016/j.nima.2021.165633>
- [22] M. Omet, A. Kuramoto, H. Hayano et al., Development and application of a frequency scan-based and a beam-based calibration method for the llrf systems at KEK STF, in *Proceedings of the 9th Annual Meeting of the Particle Accelerator Society of Japan*, Osaka, Japan, 8-11 August 2012 (PASJ, Osaka, Japan, 2012), pp. 265-268.
- [23] B. Alexander, Development of a finite state machine for the automated operation of the LLRF control at FLASH, Dissertation for the Doctoral Degree (Universitt Hamburg, Hamburg, 2007).
- [24] R. Kalt, Z.Q. Geng, RF and Beam Stability at SwissFEL, in *oral presentation of 2019 LLRF workshop*, Chicago, US, 29 September-03 October 2019 (Fermilab and Argonne National Laboratories, US, 2019).
- [25] S. N. Simrock and T. Schilcher, Transient beam loading based calibration of the vector-sum for the tesla test facility, in *Proceedings of 5th European Particle Accelerator Conf. (EPAC'96)*, Sitges, Spain, 10-14 June 1996, edited by JACoW editor team (JACoW, Sitges, Spain, 1996). Available at <https://accelconf.web.cern.ch/e96/PAPERS/THPL/THP025L.PDF>
- [26] P. Pawlik, M. Grecki and S. Simrock, Single bunch transient detection for the beam phase measurement in superconducting accelerators, in *Proceedings of 7th European Workshop on Beam Diagnostics and Instrumentation for Particle Accelerators (DIPAC2005)*, Lyon, France, 6-8 June 2005, edited by JACoW editor team (JACoW, Lyon, France, 2005), pp. 108-110. Available at <https://epaper.kek.jp/d05/PAPERS/POM031.PDF>
- [27] S. Simrock, Z. Geng, LLRF Control Applications, in *sixth International Accelerator School for Linear Colliders*, Asilomar Conference Center, Pacific Grove, California, USA, 2011, 6-17 November 2011, (Pacific Grove, California, USA, 2011).
- [28] F. Qiu, S. Michizono, T. Miura et al., Real-time cavity simulator-based low-level radio-frequency test bench and applications for accelerators. Phys. Rev. Accel. Beams **21**, 032003 (2018). DOI: <https://doi.org/10.1103/PhysRevAccelBeams.21.032003>
- [29] R. H. Fowler and L. Nordheim, Electron emission in intense electric fields, in *Proceedings of the Royal Society A*, **119**, 1928, pp. 173-181.

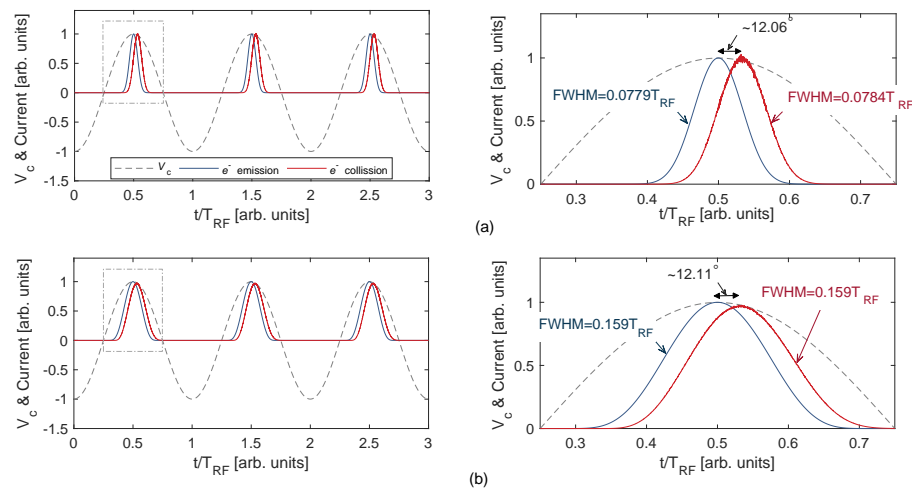


Fig. 19. (Color online) Initial FE current (dark blue) versus the FE current when the electrons collide with the outer conductor for (a) $\beta_{FN}=130$ and (b) $\beta_{FN}=1000$. The phase between the FE current and RF is $\sim 12^\circ$ (indicated by the magnified plots on the right side).

- [30] R. Xiang, A. Arnold, T. Kamps et al., Experimental studies of dark current in a superconducting rf photoinjector. *Phys. Rev. ST Accel. Beams* **17**, 043401 (2014). DOI: 10.1103/PhysRevSTAB.17.043401
- [31] J. Knobloch, *Advanced Thermometry Studies of Superconducting Radio-Frequency cavities*, Dissertation for the Doctoral Degree (Cornell University, 1997).
- [32] A. Hassanein, Z. Insepov, J. Norem et al., Ef-

- fects of surface damage on rf cavity operation. *Phys. Rev. ST Accel. Beams* **9**, 062001 (2006). <https://doi.org/10.1103/PhysRevSTAB.9.062001>
- [33] H. Padamsee and J. Knobloch, The nature of field emission from microparticles and the ensuing voltage breakdown. *AIP Conf. Proc.* **474**, 212 (1999). DOI: <https://doi.org/10.1063/1.59014>